Mapping return currents in laser-generated Z-pinch plasmas using proton deflectometry

M. J.-E. Manuel, N. Sinenian, F. H. Séguin, C. K. Li, J. A. Frenje et al.

Citation: Appl. Phys. Lett. **100**, 203505 (2012); doi: 10.1063/1.4718425
View online: http://dx.doi.org/10.1063/1.4718425
View Table of Contents: http://apl.aip.org/resource/1/APPLAB/v100/i20
Published by the American Institute of Physics.

Mapping return currents in laser-generated Z-pinch plasmas using proton deflectometry

M. J.-E. Manuel,[1] N. Sinenian,[1] F. H. Séguin,[1] C. K. Li,[1] J. A. Frenje,[1] H. G. Rinderknecht,[1] D. T. Casey,[1] A. B. Zylstra,[1] R. D. Petrasso,[1] and F. N. Beg[2]
[1]*Plasma Science and Fusion Center, MIT, Cambridge, Massachusetts 02144, USA*
[2]*Department of Mechanical and Aerospace Engineering, University of California, San Diego, California 92093-0411, USA*

(Received 21 March 2012; accepted 1 May 2012; published online 15 May 2012)

Dynamic return currents and electromagnetic field structure in laser-generated Z-pinch plasmas have been measured using proton deflectometry. Experiments were modeled to accurately interpret deflections observed in proton radiographs. Current flow is shown to begin on axis and migrate outwards with the expanding coronal plasma. Magnetic field strengths of ~1 T are generated by currents that increase from ~2 kA to ~7 kA over the course of the laser pulse. Proton deflectometry has been demonstrated to be a practical alternative to other magnetic field diagnostics for these types of plasmas. © *2012 American Institute of Physics*. [http://dx.doi.org/10.1063/1.4718425]

There has been significant effort made to measure spatial distributions of current and magnetic fields in Z-pinch plasmas.[1–3] Conventional techniques, namely Faraday rotation and B-dot probes, have limitations as wire Z-pinch plasmas have very high density in the core and significant density and temperature gradients in the coronal plasma. Proton deflectometry can provide information about current strength as well as magnetic field topology in these plasmas.

In this letter, spatially resolved measurements of dynamic currents in Z-pinch plasmas have been made using monoenergetic proton deflectometry. Plasma is created by large return currents[4] driven through the supporting stalk structure of laser-irradiated targets. The stalk ablates through ohmic heating caused by return currents which also generate azimuthal magnetic fields. The laser interaction with the target produces a positive potential[5] on the target assembly, resulting in a radial electric field on the stalk. The strength and location of these electromagnetic fields have been determined using monoenergetic proton deflectometry.

Experiments were performed at the OMEGA (Ref. 6) laser facility using the configuration shown in Figure 1(a). A thin-glass capsule filled with equimolar D^3He gas was driven by 20 beams to produce fusion protons. This implosion generates monoenergetic DD and D^3He fusion protons in a quasi-isotropic manner as demonstrated[7–10] in many experiments. The fusion burn region has an approximately Gaussian radial profile with a full-width-half-maximum of ~45 μm (Ref. 7) and a burn duration of ~150 ps. Only DD protons were used in these experiments and a sample spectrum is shown in Figure 1(b). An upshift in energy (~500 keV) is observed due to the positive potential[11,12] on the backlighter capsule itself during proton production. A detailed schematic of the target assembly is shown in Figure 1(c) with typical dimensions and materials listed. Each experiment yielded a snapshot of the resultant Z-pinch plasma dependent on the proton time-of-flight and the relative timing between backlighter and target drives. By changing the relative timing between backlighter and target drives, radiographs were taken at different points during the Z-pinch plasma evolution. Exact timing received in each experiment is assessed post-shot and fluence images are normalized for comparison between different shots. Proton radiographs were recorded on a CR-39 plastic nuclear track detector. Proton fluence and relative energy images were generated from processed[13,14] CR-39 samples.

The experimental geometry was modeled using the Geant4 (Refs. 15 and 16) framework to accurately interpret proton radiographs. Two sample synthetic radiographs are illustrated in Figure 2(a). The first case is a simple 140 μm diameter boron stalk with no fields. The stalk stops and scatters DD protons as demonstrated by the white "shadow" in the fluence image. The second Geant4 simulation example presented in Figure 2(a) has implemented axisymmetric E and B fields. A constant current I and linear charge density λ are distributed uniformly within separate cylindrical annuli around the cold stalk. This model approximates a situation

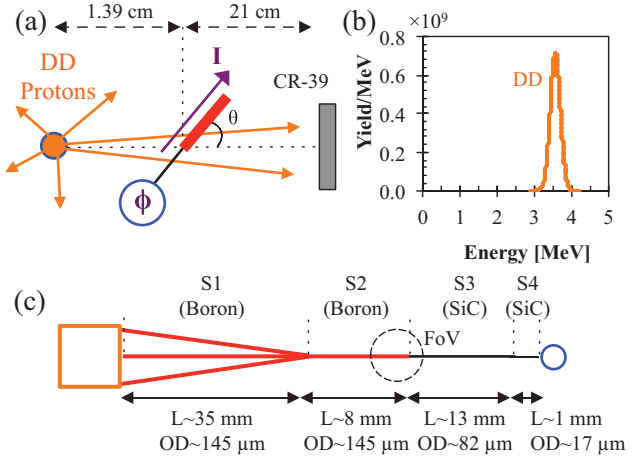

FIG. 1. (a) Experimental geometry. The stalk symmetry axis makes an angle $\theta \approx 39.4°$ with the imaging axis which is necessary for net deflections due to B fields. Residual positive charge on the target creates a potential ϕ that drives a current I up the stalk. (b) Sample fusion proton spectrum. (c) An expanded view of the stalk assembly holding the target (not to scale). Approximate lengths (L) and outer diameters (OD) are listed for the boron (B) and silicon-carbide (SiC) fiber components. The approximate field of view is indicated by the dashed circle.

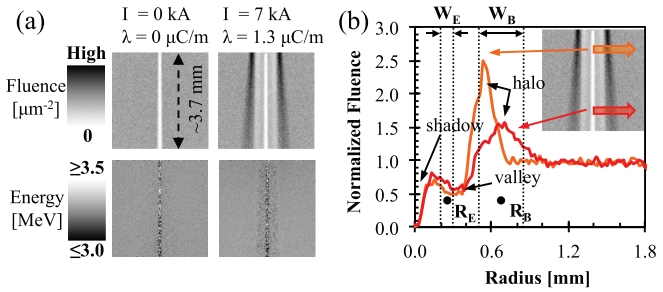

FIG. 2. (a) Synthetic proton radiographs. E and B fields are defined by a linear charge density λ and current I, respectively. (b) Fluence lineouts, indicated by arrows, of the second case in (a). The mean radii of distributed λ (R_E) and I (R_B) are shown and the widths (W_E and W_B) of the cylindrical annuli indicated by dotted lines. Qualitative lineout features are labeled.

where the current preferentially flows in the expanding hot plasma, due to lower resistivity, and the positive potential manifests as a charge imbalance. A total of six parameters characterize simulated B and E fields: the current I and charge density λ; the mean radii of each annulus, R_B and R_E; the corresponding widths, W_B and W_E. Assuming an axisymmetric structure, E fields are directed radially outward and B fields are azimuthal around the stalk and vary only as a function of radius. These independently defined parameters determine the appearance of resultant proton radiographs in a specified geometry. Any coronal-plasma non-uniformities are neglected in this analysis, however, this will be addressed in future publications.

In Figure 2(b), two fluence lineouts are shown from different positions along the stalk axis (indicated by arrows). In this simulation, $I = 7$ kA, $\lambda = 1.3$ μC/m and spatial parameters were set as follows: $R_B = 675$ μm, $R_E = 250$ μm, $W_B = 350$ μm, and $W_E = 100$ μm. An asymmetry is observed due to the differing optical characteristics at locations along the stalk. However, in many cases the qualitative features labeled in Figure 2(b) may be intuitively explained by the parameters defined in the simulation. Because the angle (θ) is not 90°, focusing optics vary along the stalk. Furthermore, to observe a net deflection due to azimuthal B fields the angle θ must be $<90°$. With the current directed away from the target, resultant B fields act to focus protons towards the stalk generating the halo, whereas the positive potential generates electric fields which deflect protons away from the stalk and produce the valley. The precise development of the halo and valley, however, is a result of the combined forces of both B and E fields. For this reason, the relative positions and magnitudes of these forces—as defined by the six input parameters—determine the characteristic features of proton radiographs in a truly coupled manner.

Target stalks were imaged on four shots at different times relative to the onset of the laser drive as indicated (•) in Figure 3(a). Both fluence $\langle N \rangle$ and energy $\langle E \rangle$ images were generated from DD-proton radiographs and are shown for each sampled time in Figure 3(b). In fluence images, darker pixels indicate higher fluence and in energy images, darker pixels indicate lower energy. Because electrons are leaving the target, a residual positive charge is left on the target and stalk with a return current directed as illustrated in Figure 1(a). During the pulse, positive charge accumulates and the position and strength of the return current evolves. In some cases, the S3 (SiC) segment of the stalk is not visible, so discussion is limited to the S2 (B) segment at the top of the images (chamber-side). Similar features are observed at the bottom (target-side) of the stalk, though the diameter, material, and optical characteristics are different.

Proton fluence images reveal dynamic E and B field structure over the duration of the laser pulse. The first image in Figure 3(b) at 1.1 ns shows no sign of the stalk shadow, but a fluence enhancement is observed in its place. This is caused by the return current flowing near the stalk surface, focusing protons to where the shadow would have been. By 1.9 ns, the valley and the halo have become well formed. At 2.4 ns, the stalk shadow has become clearly visible and all of the current flows in the coronal plasma. After the laser pulse has turned off, a strong positive charge and return current are still prevalent. In the last two radiographs, some instabilities are observed jetting out from the stalk; these stochastic features were not modeled or used in comparisons with synthetic radiographs.

An iterative procedure was implemented to infer the approximate location and strength of return currents and residual positive charge. Both synthetic and experimental fluence images were normalized to the background level for comparison and interpretation. In this way, the normalized magnitudes of characteristic features observed in fluence images were directly related to the strength of the current (I) and charge density (λ) through complex electromagnetic optics. An unique solution using this model may be found by achieving reasonable agreement between experimental and synthetic radiographs in the specified geometry. The uniform radial distributions implemented capture the dominant deflection characteristics and reproduce the data well. Investigation of higher order perturbations to the principal distribution developed herein is currently underway.

Uncertainties in measurements are estimated based on the sensitivity of synthetic data to input variations and the

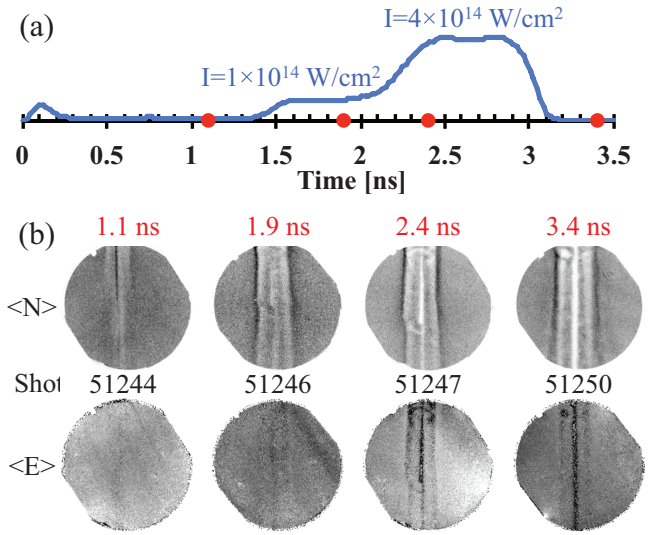

FIG. 3. (a) The picketed laser pulse used on 35 μm thick CH shells. Proton arrival times are shown by points lying on the time axis. (b) Proton fluence radiographs $\langle N \rangle$ taken at four times relative to the laser drive where darker pixels designate higher fluence. The corresponding mean energy images $\langle E \rangle$ are also shown where darker pixels indicate lower energy. (c) Comparison between synthetic (dashed) and experimental (solid) lineouts for the 1.1 ns image. (d) Comparison between synthetic (dashed) and experimental (solid) lineouts for the 2.4 ns image.

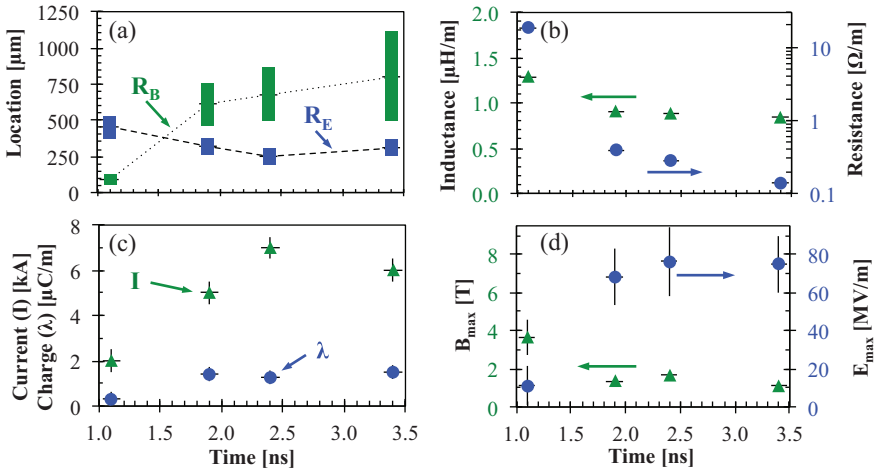

FIG. 4. Inferred values of current and charge characteristics as a function of time relative to laser onset. (a) Location and width of cylindrical annuli for currents and net charge plotted versus time. (b) Estimated inductance and resistance per unit length using the geometries shown in (a). (c) Inferred current I and charge density λ. (d) Corresponding peak field strengths.

uncertainty of experimental data due to different analysis parameters (i.e., lineout width and location). Non-axisymmetric behavior observed in experimental data also contributes some uncertainty to the inferred measurement, but those areas are not used in comparisons with synthetic radiographs. Taking these uncertainties into consideration, constant error bars are conservatively estimated to be ± 0.5 kA and ± 0.3 μC/m for the current and charge density, respectively. Uncertainties in spatial parameters $R_{B/E}$ and $W_{B/E}$ are not shown in plots, but are estimated to be $\pm$ 50 μm.

Current dynamics inferred from proton radiographs are illustrated in Figure 4(a). The current annulus, characterized by R_B and W_B, was used to calculate the inductance and resistance per unit length, and are shown in Figure 4(b) as a function of time. The coronal plasma temperature was estimated assuming that the mean expansion velocity $\left(\frac{dR_B}{dt}\right)$ was equal to the sound speed, resulting in ion temperatures of order $\sim$500 eV. To estimate resistivity, the Spitzer form ($\eta \propto ZT_e^{-3/2}$) was assumed for a fully ionized coronal Boron plasma with $T_e \sim$ 500 eV. It is important to note the low effective resistance per unit length of the plasma $\sim$0.5 Ω/m, as compared to the room temperature measurements of $\sim 10^8$ Ω/m for the Boron fiber. From these calculations, an estimated time constant ($\tau \sim$ L/R) was found to increase from $\sim$0.1 μs to $\sim$10 μs. This variability is dominated by the changing resistance of the current carrying plasma. Moreover, these time scales are much longer than any relevant plasma time scales ($\sim$ns), indicating that the current will persist well after the $\sim$3 ns laser pulse. Although, as the plasma expands and cools, the resistance will increase and the effective decay time decrease, though this does not occur during the sampled time.

Measurements of I and λ are shown in Figure 4(c). Charge accumulation increases in time eventually flattening out around $\sim$ 1.3 μC/m at 1.9 ns. Furthermore, the resultant return current increases from $\sim$2 kA to $\sim$7 kA at 2.4 ns and slightly decays a few hundred picoseconds after the laser turns off. Because the current decay time τ is long compared to the sampled time scales, the current is expected to remain after the pulse has ended. The current begins near the stalk surface and then preferentially flows outward with the expanding coronal plasma due to the reduced resistivity. Peak magnetic field magnitudes were found to decrease sharply from $\sim$4 T to $\sim$1 T and remained approximately constant throughout the sampled times.

Results presented herein provide measurements of the dynamic location of current flow in laser-generated Z-pinch plasmas. The model discussed provided an absolute measure of current and charge accumulation while capturing the dominant effects on proton deflections. Perturbations to this distribution are expected to alter the details of the observed features, but the effect on inferred magnitudes and mean locations will be minimal due to the dependence of optical characteristics on the absolute field magnitudes. Further investigation into magneto-hydrodynamic modeling of the Z-pinch plasma evolution is currently underway to determine deviations from the uniform distributions currently implemented. Moreover, for a self-consistent picture, a complete circuit model of the target-stalk-chamber system is being developed. These issues will be addressed in detail in future publications.

In summary, the feasibility of using proton deflectometry to map electric and magnetic field evolution in a "single wire"-style Z-pinch configuration has been demonstrated. The skewed angle of the stalk allowed protons to be sensitive to both self-generated electric and magnetic fields. For currents of a few kA, $\sim$3 MeV protons provided a reasonable amount of deflection without leaving the field of view. If larger currents were present, higher energy protons would be needed to properly map the field evolution. In these experiments, return currents were measured and found to increase from $\sim$2 kA to $\sim$7 kA during a picketed laser pulse. Observations made herein motivate further investigation of dynamic current flow measurements in larger machines, such as the Z-Accelerator. Furthermore, short-pulse proton radiography with Z-Beamlet could provide high temporal and spatial resolution of field structure in advanced pinch configurations at Z.

The authors express their gratitude to Andrew Sorce and Michelle Evans for extensive support in characterizing target stalks before and after the experiments. The authors also thank the engineering staff at LLE for their support. The work described here was done as part of the first author's PhD thesis and supported in part by DoE (DE-FG52-09NA29553), FSC/UR (415023-G), LLE (414090-G), LLNL (B580243), and NLUF (DE-NA0000877).

[1]F. N. Beg, A. E. Dangor, P. Lee, M. Tatarakis, S. L. Niffikeer, and M. G. Haines, "Optical and x-ray observations of carbon and aluminum fibre z-pinch plasmas," Plasma Phys. Controlled Fusion **39**(1), 0741–3335 (1997).
[2]S. N. Bland, D. J. Ampleford, S. C. Bott, A. Guite, G. N. Hall, S. M. Hardy, S. V. Lebedev, P. Shardlow, A. Harvey-Thompson, F. Suzuki *et al.*, "Use of Faraday probing to estimate current distribution in wire array Z pinches," Rev. Sci. Instrum. **77**(10), 10E315–3 (2006).
[3]V. V. Ivanov, V. I. Sotnikov, G. S. Sarkisov, T. E. Cowan, S. N. Bland, B. Jones, C. A. Coverdale, C. Deeney, P. J. Laca, A. L. Astanovitskiy *et al.*, "Dynamics of mass transport and magnetic fields in low-wire-number-array Z pinches," Phys. Rev. Lett. **97**(12), 125001 (2006).
[4]Robert F. Benjamin, Gene H. McCall, and A. Wayne Ehler, "Measurement of return current in a laser-produced plasma," Phys. Rev. Lett. **42**(14), 890–893 (1979).
[5]J. S. Pearlman and G. H. Dahlbacka, "Charge separation and target voltages in laser-produced plasmas," Appl. Phys. Lett. **31**(7), 414–417 (1977).
[6]T. R. Boehly, D. L. Brown, R. S. Craxton, R. L. Keck, J. P. Knauer, J. H. Kelly, T. J. Kessler, S. A. Kumpan, S. J. Loucks, S. A. Letzring *et al.*, "Initial performance results of the omega laser system," Opt. Commun. **133**(1–6), 495–506 (1997).
[7]C. K. Li, F. H. Séguin, J. A. Frenje, J. R. Rygg, R. D. Petrasso, R. P. J. Town, P. A. Amendt, S. P. Hatchett, O. L. Landen, A. J. Mackinnon *et al.*, "Measuring E and B fields in laser-produced plasmas with monoenergetic proton radiography," Phys. Rev. Lett. **97**(13), 135003 (2006).
[8]J. R. Rygg, F. H. Séguin, C. K. Li, J. A. Frenje, M. J.-E. Manuel, R. D. Petrasso, R. Betti, J. A. Delettrez, O. V. Gotchev, J. P. Knauer *et al.*, "Proton radiography of inertial fusion implosions," Science **319**(5867), 1223–1225 (2008).
[9]C. K. Li, F. H. Séguin, J. A. Frenje, M. Rosenberg, R. D. Petrasso, P. A. Amendt, J. A. Koch, O. L. Landen, H. S. Park, H. F. Robey *et al.*, "Charged-particle probing of x-ray-driven inertial-fusion implosions," Science **327**(5970), 1231–1235 (2010).
[10]F. H. Séguin, C. K. Li, M. J.-E. Manuel, H. G. Rinderknecht, N. Sinenian, J. A. Frenje, J. R. Rygg, D. G. Hicks, R. D. Petrasso, J. Delettrez *et al.*, "Time evolution of filamentation and self-generated fields in the coronae of directly driven inertial-confinement fusion capsules," Phys. Plasmas **19**, 012701 (2012).
[11]D. G. Hicks, C. K. Li, F. H. Séguin, A. K. Ram, J. A. Frenje, R. D. Petrasso, J. M. Soures, V. Yu Glebov, D. D. Meyerhofer, S. Roberts *et al.*, "Charged-particle acceleration and energy loss in laser-produced plasmas," Phys. Plasmas **7**(12), 5106–5117 (2000).
[12]F. H. Séguin, J. A. Frenje, C. K. Li, D. G. Hicks, S. Kurebayashi, J. R. Rygg, B. E. Schwartz, R. D. Petrasso, S. Roberts, J. M. Soures, D. D. Meyerhofer, T. C. Sangster, J. P. Knauer, C. Sorce, V. Yu. Glebov, C. Stoeckl, T. W. Phillips, R. J. Leeper, K. Fletcher, and S. Padalino, "Spectrometry of charged particles from inertial-confinement-fusion plasmas," Rev. Sci. Instrum. **74**(2), 975–995 (2003).
[13]M. J. E. Manuel, M. J. Rosenberg, N. Sinenian, H. Rinderknecht, A. B. Zylstra, F. H. Seguin, J. A. Frenje, C. K. Li, and R. D. Petrasso, "Changes in cr-39 proton sensitivity due to prolonged exposure to high vacuums relevant to the national ignition facility and omega," Rev. Sci. Instrum. **82**(9), 095110–095110–8 (2011).
[14]N. Sinenian, M. Rosenberg, M. J. E. Manuel, S. C. McDuffee, F. H. Séguin, J. A. Frenje, C. K. Li, and R. D. Petrasso, "Cr-39 track diameter response to 1-10 MeV protons for different physical etch conditions," Rev. Sci. Instrum. **82**(10), 7 (2011).
[15]S. Agostinelli, J. Allison, K. Amako, J. Apostolakis, H. Araujo, P. Arce, M. Asai, D. Axen, S. Banerjee, G. Barrand *et al.*, "G4–a simulation toolkit," Nucl. Instrum. Methods A **506**(3), 250–303 (2003).
[16]J. Allison, K. Amako, J. Apostolakis, H. Araujo, P. Arce Dubois, M. Asai, G. Barrand, R. Capra, S. Chauvie, R. Chytracek *et al.*, "Geant4 developments and applications," IEEE Trans. Nucl. Sci. **53**(1), 270–278 (2006).